

LATEX Author Guidelines for CVPR Proceedings

Anonymous CVPR submission

Paper ID *****

Abstract

The global increase in the frequency and intensity of wildfires underscores the need for advancements in fire monitoring techniques. In order to investigate deep learning approaches for detecting and tracking wildfires and the related human health impacts, we present *SmokeViz*, a large scale machine learning dataset of smoke plumes in satellite imagery. To build the dataset, we refine a set of human-generated annotations created by analysts at the National Oceanic and Atmospheric Administration. Each annotation gives a general temporal and geographical approximation of smoke plumes but at variable and, primarily, low temporal resolution. We present an innovative solution for refining the temporal and spatial resolution in the given analyst annotations by leveraging the semi-supervised method, pseudo-labeling. Unlike typical pseudo-labeling applications that aim to increase the number of labeled samples, the objective is to use pseudo-labels to refine an existing but coarse-grained set of annotations. We train a deep learning model to generate pseudo-labels that pinpoint the singular, most representative, satellite image to match the smoke annotation within the given temporal range. By identifying the most representative imagery of smoke plumes for a given smoke annotation, the study seeks to create an accurate and relevant machine learning dataset. The resulting *SmokeViz* dataset is anticipated to be an instrumental tool in developing further machine learning models and is publically available at [aws download link].

1. Introduction

In part, due to public policy, the average levels of fine particulate matter ($PM_{2.5}$) in the US have generally been declining over the past few decades[1]. Despite those improvements, the contribution of wildfire smoke to $PM_{2.5}$ concentrations in the US has been calculated to have more than doubled between 2010 to 2020, accounting for up to half of the overall $PM_{2.5}$ exposure in Western regions [2]. Increases in $PM_{2.5}$ due to wildfire smoke are concerning since ambient $PM_{2.5}$ exposure is a leading environmental risk factor for adverse

health effects and premature mortality [3]. These risks underscore the necessity for efficient and effective monitoring methods to mitigate the adverse health impacts associated with wildfire smoke.

Traditionally, wildfire monitoring has relied on ground-based methods, such as forest service patrols, manned lookout towers, and aviation surveillance [4]. While these methods provide valuable localized insights, they are constrained by geographical and logistical limitations, often failing to deliver timely and comprehensive data, especially over large and remote areas. In contrast, satellite imagery offers a vantage point that overcomes these limitations, providing continuous, wide-area coverage and real-time data crucial for assessing and responding to the health risks posed by wildfire smoke.

Satellite imagery, equipped with state-of-the-art sensors, such as the Advanced Baseline Imager (ABI) on the Geostationary Operational Environmental Satellites (GOES) [5], have revolutionized environmental monitoring. Compared to orbiting satellites such as the Suomi or Sentinel satellites, geostationary satellites maintain constant observation over a fixed area. GOES offers the advantage being able to reliably and consistently capture the dynamic behavior of wildfire smoke plumes. In turn, GOES capabilities can provide critical insights into the concentration and movement of smoke particulates, facilitating real-time assessments of air quality.

Integrating satellite imagery into wildfire smoke monitoring provides real-time data that can improve the timeliness of public health planning and response. By mapping the spread and density of smoke, health authorities can issue prompt warnings, implement evacuation protocols, and deploy resources effectively to mitigate health risks. Furthermore, long-term data gathered from satellite observations can aid in understanding the broader impacts of wildfire smoke on public health, influencing policy decisions and preventive measures.

In addition, models for real-time smoke dispersion currently have no smoke analysis product available for data assimilation [6, 7]. This can cause delayed start up times for the smoke to begin being modeled and can result in further

038

039

040

041

042

043

044

045

046

047

048

049

050

051

052

053

054

055

056

057

058

059

060

061

062

063

064

065

066

067

068

069

070

071

072

073

074

075

076

077

078

079 down-the-line errors. Providing a real-time data assimila-
 080 tion smoke product solely dependent on incoming satellite
 081 imagery has the potential to improve existing smoke disper-
 082 sion models.

083 2. Related Work

084 2.1. Numerical

085 Currently, multi-channel thresholding is a popular method
 086 to distinguish smoke pixels from pixels containing dust,
 087 clouds or other phenomenon with similar signatures [8].
 088 Thresholds are determined by using historical, labeled data
 089 to extract optimal radiance values for each channel that cor-
 090 responds with the labeled class. These methods are tuned to
 091 particular biogeographies and often have issues with gener-
 092 alization to new locations with varying fuel types [9].

093 2.2. Analyst

094 In contrast to the numerical thresholding approach, human
 095 visual inspection of satellite imagery is another commonly
 096 used method for smoke identification. Trained analyst in-
 097 spect satellite imagery and label the smoke by hand. An ex-
 098 ample of hand-labeled annotations is the National Oceanic
 099 and Atmospheric Administration (NOAA) Hazard Mapping
 100 System (HMS) fire and smoke product [10, 11]. For the
 101 HMS smoke product, trained satellite analysts use move-
 102 ment characteristics to help identify smoke by scanning
 103 through a time series of satellite imagery. When visual in-
 104 spection indicates smoke, the analyst will draw a polygon
 105 that corresponds to the geolocation and density of smoke.
 106 By design of the product, the HMS annotations have vary-
 107 ing time resolution and are released on a rolling but unde-
 108 fined schedule ranging from one to multiple times a day as
 109 observation conditions permit. This method is potentially
 110 not as scalable as an automated approach and is limited by
 111 the availability of analysts and their time.

112 NOAA manages environmental satellite programs such
 113 as the HMS program, the HMS program is an operational
 114 system that uses an aggregation of satellite data to generate
 115 active fire and smoke data. To train our model, we imple-
 116 ment a supervised learning framework that uses the HMS
 117 analyst smoke product as truth labels during the model
 118 training process.

119 HMS smoke analysis data gives the coordinates of the
 120 smoke perimeter as a polygon and classifies the smoke by
 121 density within a given time window. The time windows can
 122 range from instantaneous (same start/end time) to lengths of
 123 22 hours. While the true bounds of the smoke can change
 124 within the larger time spans, the analyst is making an ap-
 125 proximation that should reflect the smoke coverage over the
 126 duration of the time window. The density information is
 127 qualitatively determined by each analyst based on the ap-
 128 parent smoke opacity in the satellite imagery and cate-

129 rized as either light, medium or heavy as seen in figure 1a
 130 [12].

131 2.3. Deep Learning

132 To address the challenges associated with thresholding and
 133 manual labels, we can look towards innovative approaches
 134 and recent technological advancements in computer vision.
 135 Machine learning methods have shown potential in improv-
 136 ing the accuracy and efficiency of satellite-based wildfire
 137 smoke detection and monitoring. For instance, SmokeNet,
 138 uses a convolutional neural network (CNN) based frame-
 139 work to determine if a scene of MODIS satellite imagery
 140 contains smoke [13]. Another study, that looked at a singu-
 141 lar wildfire event, also used a CNN to identify smoke on a
 142 pixel-wise basis using imagery from Himawari-8 [14]. Ad-
 143 ditionally, Wen et al. developed a CNN architecture that
 144 takes GOES-East imagery as input and the HMS-generated
 145 annotations for the target labels during training [15].

146 The success of deep learning methods, such as CNNs,
 147 relies heavily on the availability of a large, representative
 148 dataset [16]. As laid out in table 1, prior studies use rela-
 149 tively small numbers of samples, from 47 [17] to 6825 [15],
 150 where one sample represents a satellite image with a singu-
 151 lar time and geolocation. In contrast, benchmark datasets
 152 for image classification contain tens of thousands (CIFAR-
 153 10 and MNIST) to millions (CIFAR-100 and ImageNet) of
 154 data samples [18–20]. Keeping in mind the correlation be-
 155 tween both the quality and quantity of data with model per-
 156 formance, we introduce the largest known smoke dataset,
 157 SmokeViz, containing over 130,000 samples.

158 Semi-supervised learning is an approach that can be used
 159 to increase the number of labeled samples in a dataset. This
 160 is done by leveraging a labeled dataset to generate new la-
 161 bels for an often larger, but unlabeled, dataset. Pseudo-
 162 labeling, a form of semi-supervised learning, uses labeled
 163 data to train an initial model, then runs that model on unla-
 164 beled data to predict pseudo-labels, and finally trains a new
 165 model using the pseudo-labels [21]. Since we do not know
 166 of any studies that have used this technique in this way, we
 167 introduce a variation of pseudo-labeling, not to increase the
 168 size, but to increase the quality of our dataset by generating
 169 pseudo-labels to select the best satellite image out of a given
 170 time-window to represent each smoke plume annotation.

171 3. Methods

172 3.1. Datasets

173 In order to take into account movement characteristics to
 174 help identify smoke, analysts use multi-frame animations
 175 of the satellite imagery. The resulting annotations primar-
 176 ily have time windows over multiple hours, with an average
 177 of 3 hours of imagery represents one smoke plume anno-
 178 tation. Since the goal of these annotations is to show the

Table 1. Comparison of different studies including method used, dataset size, satellite source, number of channels used and if classification is performed at a pixel or image level.

Reference	Method	# Samples	Satellite	# Channels	Level
[13]	CNN	6255	MODIS	5	image
[15]	CNN	6825	GOES-East	5	pixel
[14]	CNN	975	Himiwari-8	7	pixel
[17]	U-Net	47	Landsat-8	13	pixel
SmokeViz	U-Net	207,106	GOES-East/West	3	pixel

179 general coverage over that time span, as shown in figure 2,
 180 the smoke boundaries don't often match up with the satellite
 181 imagery over the entire time window. One way to approach
 182 this problem would be to use all the satellite images the
 183 analysts used as input. Since the timespans are non-uniform,
 184 this would vary the length in imagery inputs into the model,
 185 which would be difficult with a CNN architecture. More-
 186 over, this would require a large amount of additional mem-
 187 ory and computational resources. Instead of using the orig-
 188 inal analysts' many satellite image inputs to one annotated
 189 output, we develop a one-to-one input-to-output by finding
 190 the optimal singular satellite image input to represent the
 191 annotation.

192 For the set of smoke annotations, \mathcal{Y} , $y \in \mathcal{Y}$ uses one or
 193 more $x \in \mathcal{X}$ where \mathcal{X} is the entire set of satellite imagery
 194 corresponding to the set of time windows defined by the la-
 195 bels. In order to develop a one-to-one data-to-label dataset,
 196 we apply pseudo-labeling to develop a subset of \mathcal{X} , denoted
 197 as \mathcal{X}_p , that has a one-to-one ratio such that $|\mathcal{X}_p| = |\mathcal{Y}|$,
 198 where we choose the satellite image that has the maximum
 199 overlap between the geolocation of smoke in the imagery
 200 and the analyst annotation.

201 But in order to create pseudo-labels we need an initial
 202 parent model, f_o . To train f_o , we need a way of choosing
 203 $x \in \mathcal{X}$ that has a higher chance than random selection of
 204 being representative of y . Discussed in further detail in the
 205 Mie-Derived Dataset subsection, we do this by making a se-
 206 ries of physics-driven choices on which satellite and times-
 207 stamp would give the optimal angle between the sun, smoke
 208 and satellite to produce the strongest smoke signature for
 209 the geolocation and timestamp of the smoke plume. This
 210 dataset, \mathcal{X}_M tells us that if there is smoke present during
 211 the entire time window, which timestamp would give the
 212 highest smoke signal-to-noise ratio.

213 But more importantly than knowing the timestamp for
 214 maximum signal-to-noise, we want to know which image
 215 actually has smoke present within the smoke label bound-
 216 aries. We used \mathcal{X}_M to train f_o , to identify smoke in satellite
 217 imagery, and then use that f_o to create pseudo-labels of each
 218 satellite image in a given annotation's time-window. From
 219 those results, the optimal satellite image is chosen based on
 220 which image's pseudo-labels has the greatest overlap with

Table 2. To create a true color image, we use the following bands from the ABI Level 1b CONUS (ABI-L1b-RadC) product.

band	description	center $\lambda(\mu\text{m})$	resolution (km)
C01	blue visible	0.47	1
C02	red visible	0.64	0.5
C03	veggie NIR	0.865	1

the analyst annotation.

3.1.1. Satellite Imagery

The GOES satellites are operated by NOAA in order to support meteorology research and forecasting for the United States. We use the latest operational satellites, GOES-16 (East), 17 and 18 (West) that each carry the ABI, that measure 16 bands between the visible and infrared wavelengths. In improvement to the GOES predecessors, imagery is collected every 5 minutes for the contiguous United States and every 10 minutes for the full disk. Using PyTroll, a Python framework for processing satellite data [22], we input bands 1-3 (Table 2) to a GOES specific true color composite algorithm [23] to develop a, 1km resolution, true color image representation, similar to what is seen by HMS analysts. As discussed in further detail in the next section, the highest signal-to-noise ratio will come from the smallest wavelengths of light, larger wavelengths have lower smoke signal and higher noise (figure 5). For that reason, we only include the first 3 out of 16 available bands of data.

3.1.2. Mie-Derived Dataset

We used a physics-informed approach in selecting the initial GOES dataset, \mathcal{X}_M , which we call the Mie-derived dataset, for training an initial parent model, f_o , where if \mathcal{X} represents all the GOES imagery corresponding to the HMS smoke annotation time window, $\mathcal{X}_M \subset \mathcal{X}$. Prior GOES ABI datasets for machine learning applications often include data from only one of the two GOES-series satellites, commonly opting for GOES-East [15], [24], [25]. Rather than using one satellite or the cumulative data from both GOES-West and GOES-East images, we select between one or the other based on the solar zenith angle. For smoke iden-

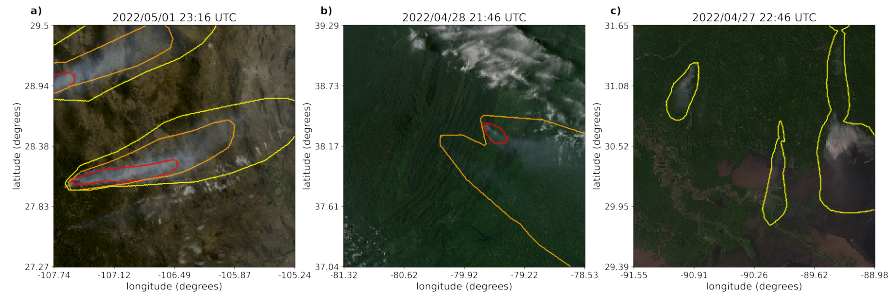


Figure 1. Satellite imagery captured by GOES-East within a few days of each other. The yellow, orange and red contours indicate the extent of light, medium and heavy density smoke. a) shows a canonical example of a smoke plume. b) and c) show observable variations in the density labels.

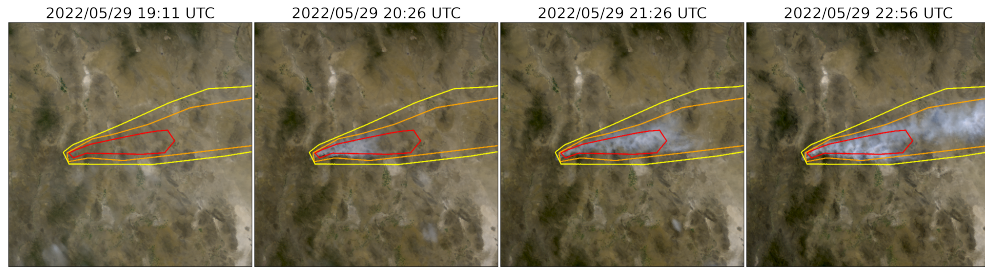


Figure 2. True color GOES-East imagery from May 2022, Southeast New Mexico (31°N , 100°W) during the start of the Foster Fire. The red, orange and yellow lines represent the heavy, medium and low density HMS smoke annotations that span 19:10–23:00 UTC.

52 tification, this approach can achieve a much higher signal-to-noise than imaging the earth's surface from an arbitrary
53 angle. The elastic scattering of light is the primary mechanism
54 to account for - while the atmosphere is composed of
55 molecules with size $< 1\text{nm}$, smoke particles can vary from
56 100 nm – $10 \mu\text{m}$ in diameter, d . The GOES ABI covers
57 spectral bands from $0.47 \mu\text{m} – 13.3 \mu\text{m}$, so atmospheric
58 and smoke particle sizes occupy two very different regimes
59 with respect to the imaging wavelength λ . In the extreme
60 limit of $\lambda \gg d$, the physics of scattering of light off a small
61 sphere is captured by Rayleigh scattering. This process has
62 two critical consequences: (1) the scattering cross section of
63 light is strongly wavelength dependent (scaling with λ^{-4}),
64 meaning that photons with wavelength closer to the ultraviolet
65 are scattered more strongly than infrared photons. (2) the
66 scattering cross section scales with an angular dependent
67 cross section of $(1 + \cos^2 \theta)$. Scattered photons follow
68 the emission distribution of a radiating dipole, scattering
69 more strongly in the forward and backwards directions
70 ($\theta = 0, \pi$) than orthogonal to the direction of propagation
71 ($\theta = \pi/2, 3\pi/2$), see figure 3 for a Rayleigh scattering
72 schematic.
73

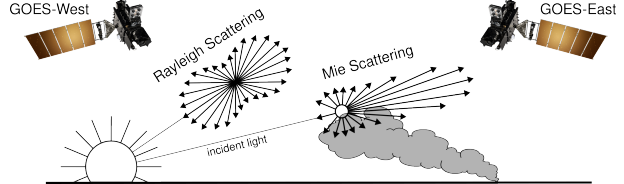


Figure 3. If the particle size is $< \frac{1}{10}$ the wavelength of the interacting light, then the primary scattering will be Rayleigh. Mie scattering is the predominant scattering mechanism when the particle size is larger than the wavelength of light. This schematic demonstrates that when the sun is setting in the West, the Mie scattering will predominately forward scatter towards GOES-East.

The significance of these scalings is that the observer, or detector, will receive blue photons in most directions orthogonal to the source. Equivalently, photons traveling colinearly with line of sight to the emission source will mostly have wavelengths in the infrared band. In the converse regime of $d > \lambda$, the elastic scattering of light against matter is modeled through Mie scattering. In comparison to Rayleigh scattering, Mie scattering is largely wavelength-independent and has a more complicated radiation pattern

274
275
276
277
278
279
280
281
282



Figure 4. True color GOES-West (left) and GOES-East (right) imagery from April 24th, 2022 in Durango, Mexico. The images were taken ~ 1.5 hours before sunset (01:43 UTC) for this geolocation and time of year.

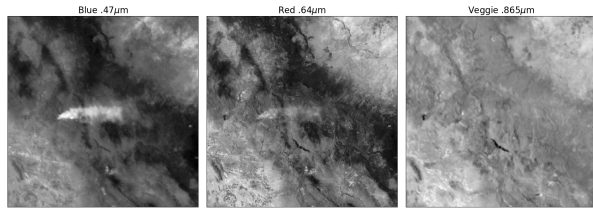


Figure 5. Three bands of GOES-East data are the raw input to generate a true color image. These plots show variations in the signal-to-noise ratio for smoke detection in relation to the λ of light being measured.

where the cross section has a maximal amplitude in the forward direction. An observer downstream of this scatterer will collect more photons than one positioned directly behind it. In the context of smoke identification, a sunrise or sunset will lead to a higher Mie scattered signal in GOES-West and GOES-East respectively, as shown with a smoke plume producing a stronger signal in GOES-East imagery near sunset in figure 4.

Smoke identification therefore amounts to extracting a signal of $d > \lambda$ photons from the $\lambda \gg d$ background. Positioning a detector along line of sight to the scatterer will result in a higher signal from smoke particles (figure 3). Filtering the imaged wavelength can enhance this signal; photons collected in the blue spectrum will have a naturally lower background along the line of sight to the illumination source due to their high level of Rayleigh scattering as. Therefore, as demonstrated in figure 5, this configuration results in the highest signal to noise imaging for smoke particles.

Based solely on these criteria, the optimal strategy would be to pull data from GOES-West right after sunrise and from GOES-East right before sunset. Another factor to consider is that the time when the sun is in optimal alignment with

the satellite for smoke detection coincides with when solar zenith angle is close to 90°. Larger angles between the satellite and sun result in an increase in noise due to increased atmospheric interactions [26]. To reduce the noise from large solar zenith angles, if given multiple frames to choose from, we choose the image with the largest solar zenith angle that is $< 88^\circ$.

The resulting image selection process takes into account atmospheric properties and light scattering physics to generate an estimate of which singular satellite image within the analyst time-window could give the highest smoke signal-to-noise ratio. The resulting Mie-derived dataset, $\mathcal{X}_M = \{X_M, Y\}$, was then used to train a model, f_o , that would generate N pseudo-labels, y^* , for every sample, where N is determined by how many images, taken at a 10 minute interval, fit within the analyst time-window for that sample. Chosen from the N images, x_p is the image with the highest alignment between the f_o prediction of smoke, y^* , in the image and the HMS analysts' annotation y .

3.1.3. Thermometer Encoding Smoke Densities

One of the challenges introduced with using human generated qualitative smoke densities was that, as seen in figure 1b and 1c, there are variations in what is labeled as heavy or light density smoke. More generally, reproducing qualitative metrics with quantitative algorithms is a challenging problem, but we apply mathematical approaches that mitigate some of the underlying complications of our specific problem. Despite the smoke densities introduce qualitative complexities, we decided that the density approximations were important to use in our dataset because of the differences in signatures the densities produce. Within the satellite imagery, the appearance of a light density smoke plume will look significantly different than a heavy density smoke plume as seen in figure 1. Additionally, a light density smoke plume is expected to be more challenging to detect since it is easier for it to be misclassified as not smoke. During the training process, the separate density categories allows us to deferentially weight the penalization given to the model for incorrect classifications based on category. For example, the model can be given a small penalization for misclassifying light smoke as not smoke while given a higher penalization for misclassifying heavy smoke as not smoke.

In addition to the densities being ordered and categorical, the differences between the density categories are not evenly distributed by a given metric, such as PM_{2.5} density. The intervals between densities being unknown along with the hierarchical nature of the density labels makes the labels ordinal instead of just categorical. This data property allows us to use thermometer encoding [27], which leverages the idea that heavy density smoke includes both medium and light density smoke, that heavy density smoke is closer to medium than it is to light, and automatically weights the

358 loss functions and incorporates the ranked ordering of the
 359 densities. As seen in Table 3, one-hot encoding, commonly
 360 used for categorical data, doesn't take ordinal properties of
 361 the data into consideration.

Table 3. A comparison of one-hot encoding used for categorical data to thermometer encoding for ordinal data.

category	one-hot	thermometer
No Smoke	[0 0 0]	[0 0 0]
Light	[0 0 1]	[0 0 1]
Medium	[0 1 0]	[0 1 1]
Heavy	[1 0 0]	[1 1 1]

362 3.1.4. Pseudo-label Dataset

363 We implement a deep learning architecture that uses the en-
 364 coder from EfficientNetV2 [28] and a semantic segmen-
 365 tation classifier from the DeepLabV3 model [29]. Transfer
 366 learning has shown to reduce the time and resources needed
 367 to train a model by leveraging information from pre-trained
 368 models [30], [31]. We initialize the values of our model
 369 weights using the pre-trained values originally trained on
 370 the ImageNet dataset [20], containing 1.2 million images
 371 and 1000 categories. Our model was developed using the
 372 Segmentation Models PyTorch package [32] that was writ-
 373 ten as a high level API for implementing models for seman-
 374 tic segmentation problems. We input 256x256x3 snapshots
 375 of 1km resolution true color GOES imagery that contains
 376 smoke and output a 256x256x3 classification map that pre-
 377 dicted if a pixel contains smoke and if so, what the density
 378 of that smoke is. As mentioned earlier, we apply the ther-
 379 mometer encoding shown in table 3 to encode the smoke
 380 densities and apply binary cross entropy as the loss func-
 381 tion per density of smoke.

382 The dataset, \mathcal{X}_M , contains 207,106 samples as shown in
 383 the dataset split in table 4.

Table 4. Dataset split for \mathcal{X}_M and \mathcal{X}_p , samples for 2024 go up to
 November 1st. We use an entire year of data for both validation
 and testing sets to capture year-long wildfire trends.

dataset	\mathcal{X}_M	\mathcal{X}_p	years
training	165,609	144,225	2018-2021, 2024
validation	20,056	19,223	2023
testing	21,541	16,855	2022

384 To determine which image out of the relevant imagery
 385 for the given time window best represents the analyst anno-
 386 tation, we implement a greedy algorithm by running f_o on
 387 each x to generate a pseudo-label, y^* . The output of f_o , y^*
 388 give predictions on if smoke is in the image, and if there is
 389 smoke, where the smoke is in that image and the density of

390 that smoke. y^* serve as pseudo-labels for each density of
 391 smoke and are compared to the analyst annotations, y . To
 392 compare y^* and y , we calculate the IoU using the total set
 393 of pixels for y^* at that density of smoke and the entire set of
 394 pixels for y for a particular smoke density in each image as
 395 shown in equation 1. The image with the highest IoU score
 396 is chosen as the image, x_p , that best represents the analyst
 397 smoke annotation, y . Often used for pseudo-labeling, a con-
 398 fidence threshold value is defined to determine if a pseudo-
 399 label should be included in a dataset [33]. We chose a
 400 confidence threshold that would include the sample, x_p , in
 401 \mathcal{X}_p if the maximum overall IoU (equation 1) between y^*
 402 and y over all densities was over 0.01.

$$IoU_{\text{overall}} = \frac{\sum_{i=\text{light}}^{\text{heavy}} |y_i \cap y_i^*|}{\sum_{i=\text{light}}^{\text{heavy}} |y_i| \cup |y_i^*|} \quad (1)$$

We use \mathcal{X}_p to train an additional child model, f_c in order to assess if training with \mathcal{X}_p can produce a more robust semantic segmentation model compared to training on \mathcal{X}_M . We use the same dataset split method and model setup but change \mathcal{X}_M to \mathcal{X}_p to train f_c .

3.2. Benchmark Models

While this dataset is anticipated to be primarily useful for solving various wildfire smoke applications, this dataset could be a uniquely insightful test case for remote sensing semantic segmentation. Many deep learning satellite image datasets are focused on objects with sharp contrasts such as crops [34], human infrastructure [35], or even clouds over oceans [36] [37], but smoke has indistinct boundaries that often fade both spatially and temporally.

We benchmark the SmokeViz dataset, \mathcal{X}_p by varying the semantic segmentation classification heads. We train Linknet [38], PSPNet [39] and Ma-net [40] using the same encoder used for f_c and f_o , EfficientNetV2. Each model is trained over 100 epochs using a batch size of 32 and the Adam optimizer on 8 Nvidia P100 GPUs allocating 10GB of memory over 12 hours of allotted training time.

4. Results

To interpret the performance of f_o , we report the IoU metrics in table 5 that were computed by running f_o and f_c on \mathcal{X}_M and \mathcal{X}_p . For each density, we calculate the IoU using the total set of pixels that f_o predicts as that density of smoke and the entire set of pixels labeled by the analyst as a particular smoke density over all imagery contained in the testing dataset. Additionally, we compute the overall IoU for all densities by first computing the number of pixels that intersect their corresponding density and divide that by the

Table 5. IoU results per density of smoke and over all densities using f_o and f_c with \mathcal{X}_M and \mathcal{X}_p .

	f_o		f_c	
	\mathcal{X}_M	\mathcal{X}_p	\mathcal{X}_M	\mathcal{X}_p
Heavy	0.278	0.368	0.218	0.411
Medium	0.310	0.417	0.319	0.484
Light	0.480	0.585	0.491	0.660
Overall	0.430	0.533	0.438	0.607

435 total number of pixels that make up the union of model predicted and analyst labeled smoke in the testing dataset.
 436

437 An illustration of a pseudo-label picked image better representing the analyst annotation when compared to the Mie-
 438 derived image selection is evident in Figure 6, where the heavy density smoke IoU increases from 0.01 to 0.59. The
 439 analyst annotation for these densities cover 5 hours of im-
 440 agery, the Mie-derived selection optimizes for the image closest to sunrise while the pseudo-label image selection
 441 chooses the image with the highest overlap between the
 442 pseudo-label and the analyst annotation. The figure also
 443 illustrates how using a deep learning model can provide
 444 higher time resolution and give a dynamic representation
 445 of smoke over time.
 446

447 To get an idea on how f_c compares to the HMS analyst
 448 annotations we show a series of samples from \mathcal{X}_p in figure
 449 6. The examples give a qualitative representation of how the
 450 predictions from f_c can provide more detailed boundaries of
 451 smoke densities than the HMS annotations do.
 452

453 Table 6. Comparison of semantic segmentation model IoU performance on \mathcal{X}_p .

	DLV3+	MANet	PSPNet	Linknet
Heavy	0.411	0.336	0.355	0.324
Medium	0.484	0.487	0.502	0.456
Light	0.662	0.675	0.690	0.662
Overall	0.607	0.615	0.626	0.601

454 The results for the benchmarking models (table 6) show
 455 similar performance across the models. DeepLabV3+ (f_c)
 456 gives the highest heavy density smoke IoU value, while
 457 PSPNet gives the highest overall IoU score.
 458

5. Limitations

459 One of the concerns that comes with using pseudo-labeling
 460 methods is that you can perpetuate biases from the parent
 461 model into subsequent child models. Due to the increase in
 462 detectable forward scattered light off smoke particular matter,
 463 we expect the model to have a bias towards producing a
 464 higher success rate for smoke detection at larger solar zenith

angles. The original HMS annotations do not distinguish by type of fire and include a large representation of controlled agricultural burns. This can be a limitation to consider if the dataset is being trained to target detection of large wildfires. All these limitations are discussed and analyzed further in the Appendix. Additional work should be done to analyze the performance of SmokeViz derived models on dust vs smoke.
 465
 466
 467
 468
 469
 470
 471
 472

6. Conclusion

473 In this study, we have refined an existing dataset originally
 474 curated by NOAA’s HMS team, transforming it from a many-to-one imagery-to-annotation format to a more succinct,
 475 one-to-one satellite image-to-annotation dataset. The
 476 initial HMS dataset provided a general approximation of
 477 where smoke had been present for a given time window,
 478 though it did not guarantee the actual existence of smoke in
 479 the labeled pixels during the given times. Our goal was to
 480 create a dataset that could be used, along with additional ap-
 481 plications, to train a model to detect wildfire smoke in real-
 482 time on an image-by-image level. The Mie-derived dataset
 483 selection process determined that if smoke was present,
 484 what timestamp within the analyst time window would the
 485 give the highest smoke signal-to-noise ratio. While optimiz-
 486 ing for being able to detect smoke, if it is present, the Mie-
 487 dataset selection had no metric to determine if the smoke
 488 was effectually present in the selected image. Since many of
 489 the images within the HMS time-window either contained
 490 no smoke at all or the smoke was not contained within
 491 the geospatial bounds of the annotations, the Mie-derived
 492 dataset contained a large number of mislabeled samples.
 493 Discrepancies between data and labels can be detrimental
 494 towards the model’s capacity to improve on feature repre-
 495 sentations in the target domain. During model training, the
 496 penalization of accurate predictions can inadvertently intro-
 497 duce biases towards misclassifying noise as meaningful sig-
 498 nal.
 499

500 To improve the dataset’s capacity to accurately represent
 501 wildfire smoke plumes, we train a parent machine learning
 502 model, f_o , using the Mie-derived dataset, \mathcal{X}_M , and run it
 503 on the relevant satellite images within the time-frame. The
 504 image with the maximum IoU score between the model’s
 505 smoke predictions, or pseudo-label, and the analyst smoke
 506 annotations are used to create the pseudo-label generated
 507 dataset, \mathcal{X}_p . We then train a child model, f_c , using \mathcal{X}_p and
 508 test f_o and f_c on both the 2022 testing sets from \mathcal{X}_M and
 509 \mathcal{X}_p . The results reported in table 5 suggest that \mathcal{X}_p was able
 510 to train a better performing model, f_c , that gave higher IoU
 511 metrics on both dataset’s testing sets in comparison to the
 512 original parent model, f_o .
 513

514 The result of this study is a representative dataset,
 515 SmokeViz, that can be used to train machine learning mod-
 516 els for various wildfire smoke applications. A future goal is
 517

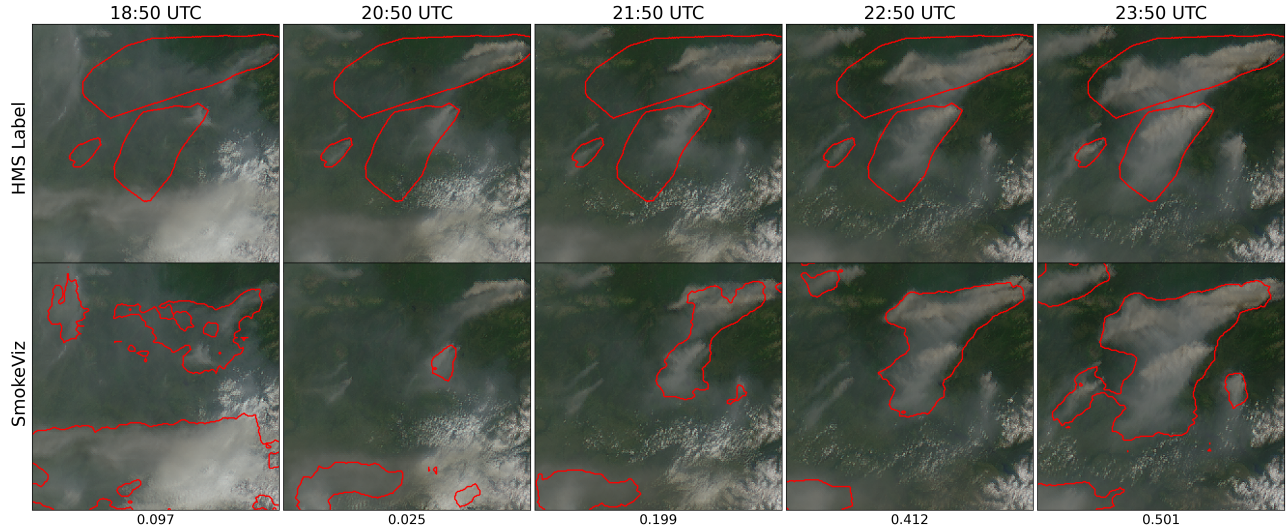


Figure 6. GOES-West imagery showing smoke on June 8th, 2022 in Alaska where, at this geolocation, daylight was between 12:43-7:53 UTC. The HMS smoke annotations (top row) span from 18:50 to 23:50 UTC and are compared to the f_c generated pseudo-labels (bottom row). The first column would be the GOES imagery selected for \mathcal{X}_M since it is closest to sunrise. The last column was selected for \mathcal{X}_p since it had the highest IoU value between the pseudo-label and analyst annotation.

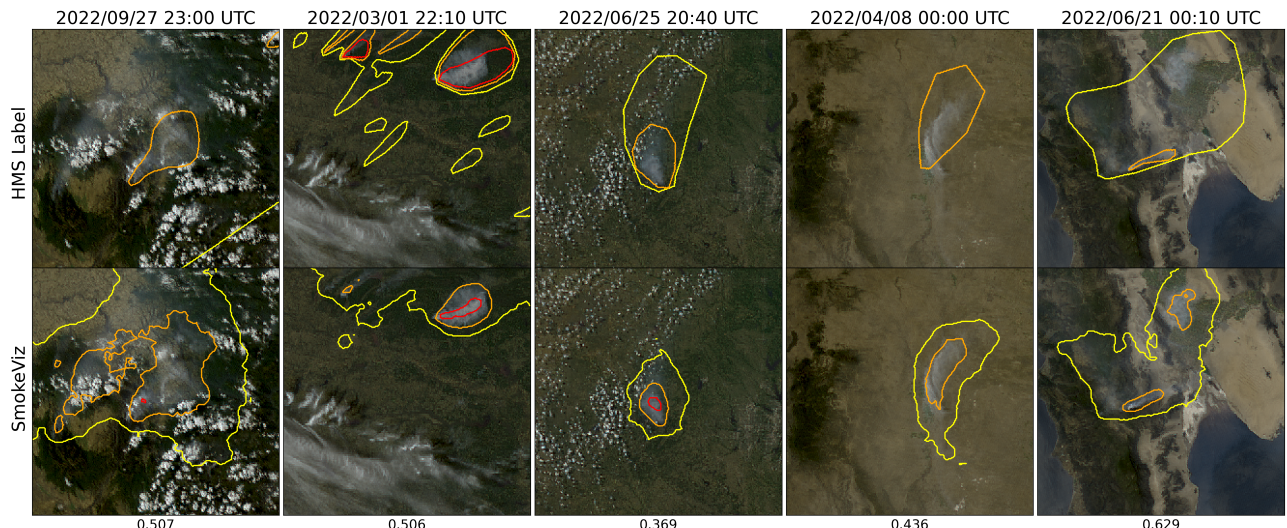


Figure 7. Examples of HMS annotations (top row) vs f_c output (bottom row) on \mathcal{X}_p samples.

517 to produce a robust and reliable machine learning based
 518 approach for detecting wildfires using satellite imagery. That
 519 information can be used for wildfire detection and moni-
 520 toring in along with a highly needed smoke product for
 521 data assimilation into smoke dispersion models. Addi-
 522 tionally, this dataset can be used as a benchmark for how well
 523 remote sensing segmentation models can perform on dis-
 524 persed edges such as smoke. On a broader scale, we show
 525 how pseudo-labeling can be used to optimize a dataset when
 526 the resolution for the data and corresponding labels do not
 527 match. This could be useful in similar applications involv-

528 ing time-series/video data with a singular label where the
 529 data can be compressed while still remaining representative
 530 of the label.

References

- [1] J. E. Aldy, M. Auffhammer, M. Cropper, A. Fraas, and R. Morgenstern, “Looking back at 50 years of the clean air act,” *Journal of Economic Literature*, vol. 60, no. 1, pp. 179–232, 2022. 1
- [2] M. Burke, A. Driscoll, S. Heft-Neal, J. Xue, J. Burney, and M. Wara, “The changing risk and burden of wildfire in the

- 538 united states," *Proceedings of the National Academy of Sciences*, vol. 118, no. 2, p. e2011048118, 2021. 1
- 539
- 540 [3] E. Gakidou, A. Afshin, A. A. Abajobir, K. H. Abate, C. Abbafati, K. M. Abbas, F. Abd-Allah, A. M. Abdulle, S. F. Abera, V. Aboyans, *et al.*, "Global, regional, and national comparative risk assessment of 84 behavioural, environmental and occupational, and metabolic risks or clusters of risks, 1990–2016: a systematic analysis for the global burden of disease study 2016," *The Lancet*, vol. 390, no. 10100, pp. 1345–1422, 2017. 1
- 541
- 542 [4] R. S. Allison, J. M. Johnston, G. Craig, and S. Jennings, "Airborne optical and thermal remote sensing for wildfire detection and monitoring," *Sensors*, vol. 16, no. 8, p. 1310, 2016. 1
- 543
- 544 [5] S. J. Goodman, T. J. Schmit, J. Daniels, and R. J. Redmon, *The GOES-R series: a new generation of geostationary environmental satellites*. Elsevier, 2019. 1
- 545
- 546 [6] E. James, R. Ahmadov, and G. A. Grell, "Realtime wildfire smoke prediction in the united states: The hrrr-smoke model," in *EGU General Assembly Conference Abstracts*, p. 19526, 2018. 1
- 547
- 548 [7] R. Ahmadov, H. Li, J. Romero-Alvarez, J. Schnell, S. Bhimireddy, E. James, K. Y. Wong, M. Hu, J. Carley, P. Bhattacharjee, *et al.*, "Forecasting smoke and dust in noaa's next-generation high-resolution coupled numerical weather prediction model," tech. rep., Copernicus Meetings, 2024. 1
- 549
- 550 [8] T. X.-P. Zhao, S. Ackerman, and W. Guo, "Dust and smoke detection for multi-channel imagers," *Remote Sensing*, vol. 2, no. 10, pp. 2347–2368, 2010. 2
- 551
- 552 [9] T. Randriambelo, S. Baldy, M. Bessafi, M. Petit, and M. Despinoy, "An improved detection and characterization of active fires and smoke plumes in south-eastern africa and madagascar," *International Journal of Remote Sensing*, vol. 19, no. 14, pp. 2623–2638, 1998. 2
- 553
- 554 [10] D. McNamara, G. Stephens, M. Ruminski, and T. Kasheta, "The hazard mapping system (hms) - noaa's multi-sensor fire and smoke detection program using environmental satellites," *Conference on Satellite Meteorology and Oceanography*, 01 2004. 2
- 555
- 556 [11] W. Schroeder, M. Ruminski, I. Csiszar, L. Giglio, E. Prins, C. Schmidt, and J. Morissette, "Validation analyses of an operational fire monitoring product: The hazard mapping system," *International Journal of Remote Sensing*, vol. 29, no. 20, pp. 6059–6066, 2008. 2
- 557
- 558 [12] NOAA, "Hazard mapping system fire and smoke product." 2
- 559
- 560 [13] R. Ba, C. Chen, J. Yuan, W. Song, and S. Lo, "Smokenet: Satellite smoke scene detection using convolutional neural network with spatial and channel-wise attention," *Remote Sensing*, vol. 11, no. 14, p. 1702, 2019. 2, 3
- 561
- 562 [14] A. Larsen, I. Hanigan, B. J. Reich, Y. Qin, M. Cope, G. Morgan, and A. G. Rappold, "A deep learning approach to identify smoke plumes in satellite imagery in near-real time for health risk communication," *Journal of exposure science & environmental epidemiology*, vol. 31, no. 1, pp. 170–176, 2021. 2, 3
- 563
- 564
- 565 [15] J. Wen and M. Burke, "Wildfire smoke plume segmentation using geostationary satellite imagery," *ArXiv*, vol. abs/2109.01637, 2021. 2, 3
- 566
- 567 [16] C. Sun, A. Shrivastava, S. Singh, and A. Gupta, "Revisiting unreasonable effectiveness of data in deep learning era," in *Proceedings of the IEEE international conference on computer vision*, pp. 843–852, 2017. 2
- 568
- 569 [17] Z. Wang, P. Yang, H. Liang, C. Zheng, J. Yin, Y. Tian, and W. Cui, "Semantic segmentation and analysis on sensitive parameters of forest fire smoke using smoke-unet and landsat-8 imagery," *Remote Sensing*, vol. 14, no. 1, p. 45, 2022. 2, 3
- 570
- 571 [18] A. Krizhevsky, G. Hinton, *et al.*, "Learning multiple layers of features from tiny images," 2009. 2
- 572
- 573 [19] L. Deng, "The mnist database of handwritten digit images for machine learning research [best of the web]," *IEEE signal processing magazine*, vol. 29, no. 6, pp. 141–142, 2012. 2
- 574
- 575 [20] J. Deng, W. Dong, R. Socher, L.-J. Li, K. Li, and L. Fei-Fei, "Imagenet: A large-scale hierarchical image database," in *2009 IEEE conference on computer vision and pattern recognition*, pp. 248–255, Ieee, 2009. 2, 6
- 576
- 577 [21] D.-H. Lee, "Pseudo-label : The simple and efficient semi-supervised learning method for deep neural networks," *ICML 2013 Workshop : Challenges in Representation Learning (WREPL)*, 07 2013. 2
- 578
- 579 [22] M. Raspaud, D. Hoese, A. Dybbroe, P. Lahtinen, A. Devasthale, M. Itkin, U. Hamann, L. Ø. Rasmussen, E. S. Nielsen, T. Leppelt, *et al.*, "Pytroll: An open-source, community-driven python framework to process earth observation satellite data," *Bulletin of the American Meteorological Society*, vol. 99, no. 7, pp. 1329–1336, 2018. 3
- 580
- 581 [23] M. Bah, M. Gunshor, and T. Schmit, "Generation of goes-16 true color imagery without a green band," *Earth and Space Science*, vol. 5, no. 9, pp. 549–558, 2018. 3
- 582
- 583 [24] T. C. Phan and T. T. Nguyen, "Remote sensing meets deep learning: exploiting spatio-temporal-spectral satellite images for early wildfire detection," 2019. 3
- 584
- 585 [25] Y. Lee, C. D. Kummerow, and I. Ebert-Uphoff, "Applying machine learning methods to detect convection using geostationary operational environmental satellite-16 (goes-16) advanced baseline imager (abi) data," *Atmospheric Measurement Techniques*, vol. 14, no. 4, pp. 2699–2716, 2021. 3
- 586
- 587 [26] A. Royer, P. Vincent, and F. Bonn, "Evaluation and correction of viewing angle effects on satellite measurements of bidirectional reflectance," *Photogrammetric engineering and remote sensing*, vol. 51, no. 12, pp. 1899–1914, 1985. 5
- 588
- 589 [27] J. Buckman, A. Roy, C. Raffel, and I. Goodfellow, "Thermometer encoding: One hot way to resist adversarial examples," in *International conference on learning representations*, 2018. 5
- 590
- 591 [28] M. Tan and Q. Le, "Efficientnetv2: Smaller models and faster training," in *International conference on machine learning*, pp. 10096–10106, PMLR, 2021. 6
- 592
- 593 [29] L.-C. Chen, G. Papandreou, I. Kokkinos, K. Murphy, and A. L. Yuille, "Deeplab: Semantic image segmentation with deep convolutional nets, atrous convolution, and fully connected crfs," *IEEE transactions on pattern analysis and machine intelligence*, vol. 40, no. 4, pp. 834–848, 2017. 6
- 594
- 595
- 596
- 597
- 598
- 599
- 600
- 601
- 602
- 603
- 604
- 605
- 606
- 607
- 608
- 609
- 610
- 611
- 612
- 613
- 614
- 615
- 616
- 617
- 618
- 619
- 620
- 621
- 622
- 623
- 624
- 625
- 626
- 627
- 628
- 629
- 630
- 631
- 632
- 633
- 634
- 635
- 636
- 637
- 638
- 639
- 640
- 641
- 642
- 643
- 644
- 645
- 646
- 647
- 648
- 649
- 650
- 651

- 652 [30] J. Yosinski, J. Clune, Y. Bengio, and H. Lipson, “How trans-
 653 ferable are features in deep neural networks?,” *Advances in*
 654 *neural information processing systems*, vol. 27, 2014. 6
- 655 [31] A. Sharif Razavian, H. Azizpour, J. Sullivan, and S. Carls-
 656 son, “Cnn features off-the-shelf: an astounding baseline for
 657 recognition,” in *Proceedings of the IEEE conference on com-*
 658 *puter vision and pattern recognition workshops*, pp. 806–
 659 813, 2014. 6
- 660 [32] P. Iakubovskii, “Segmentation models pytorch.” https://github.com/qubvel/segmentation_models.pytorch, 2019. 6
- 663 [33] R. E. Ferreira, Y. J. Lee, and J. R. Dórea, “Using pseudo-
 664 labeling to improve performance of deep neural networks
 665 for animal identification,” *Scientific Reports*, vol. 13, no. 1,
 666 p. 13875, 2023. 6
- 667 [34] J. Jakubik, S. Roy, C. Phillips, P. Fraccaro, D. God-
 668 win, B. Zadrozny, D. Szwarcman, C. Gomes, G. Nyir-
 669 jesy, B. Edwards, *et al.*, “Foundation models for generalist
 670 geospatial artificial intelligence. arxiv 2023,” *arXiv preprint*
 671 *arXiv:2310.18660*. 6
- 672 [35] S. Zorzi, S. Bazrafkan, S. Habenschuss, and F. Fraundor-
 673 fer, “Polyworld: Polygonal building extraction with graph
 674 neural networks in satellite images,” in *Proceedings of the*
 675 *IEEE/CVF Conference on Computer Vision and Pattern*
 676 *Recognition*, pp. 1848–1857, 2022. 6
- 677 [36] A. Kitamoto, J. Hwang, B. Vuillod, L. Gautier, Y. Tian,
 678 and T. Clanuwat, “Digital typhoon: Long-term satellite im-
 679 age dataset for the spatio-temporal modeling of tropical cy-
 680 clones,” *Advances in Neural Information Processing Sys-*
 681 *tems*, vol. 36, 2024. 6
- 682 [37] B. Stevens, S. Bony, H. Brogniez, L. Hentgen, C. Ho-
 683 henegger, C. Kiemle, T. S. L’Ecuyer, A. K. Naumann,
 684 H. Schulz, P. A. Siebesma, *et al.*, “Sugar, gravel, fish and
 685 flowers: Mesoscale cloud patterns in the trade winds,” *Quar-*
 686 *terly Journal of the Royal Meteorological Society*, vol. 146,
 687 no. 726, pp. 141–152, 2020. 6
- 688 [38] A. Chaurasia and E. Culurciello, “Linknet: Exploiting en-
 689 coder representations for efficient semantic segmentation,”
 690 in *2017 IEEE visual communications and image processing*
 691 (*VCIP*), pp. 1–4, IEEE, 2017. 6
- 692 [39] H. Zhao, J. Shi, X. Qi, X. Wang, and J. Jia, “Pyramid scene
 693 parsing network,” in *Proceedings of the IEEE conference*
 694 *on computer vision and pattern recognition*, pp. 2881–2890,
 695 2017. 6
- 696 [40] T. Fan, G. Wang, Y. Li, and H. Wang, “Ma-net: A multi-
 697 scale attention network for liver and tumor segmentation,”
 698 *IEEE Access*, vol. 8, pp. 179656–179665, 2020. 6